Appl. Math. Mech. -Engl. Ed.

Applied Mathematics and Mechanics (English Edition)

https://doi.org/10.1007/s10483-020-2587-8

Nonlinear dynamic analysis of moving bilayer plates resting on elastic foundations*

M. ESMAEILZADEH[1], M. KADKHODAYAN[2,†], S. MOHAMMADI[1], G. J. TURVEY[3]

1. Department of Mechanical Engineering, Mashhad Branch, Azad University, Mashhad 9187144123, Iran;
2. Department of Mechanical Engineering, Ferdowsi University of Mashhad, Mashhad 9177948944, Iran;
3. Engineering Department, Lancaster University, Bailrigg, Lancaster LA1 4YR, U. K.

(Received Aug. 25, 2019 / Revised Dec. 7, 2019)

Abstract The aim of this study is to investigate the dynamic response of axially moving two-layer laminated plates on the Winkler and Pasternak foundations. The upper and lower layers are formed from a bidirectional functionally graded (FG) layer and a graphene platelet (GPL) reinforced porous layer, respectively. Henceforth, the combined layers will be referred to as a two-dimensional (2D) FG/GPL plate. Two types of porosity and three graphene dispersion patterns, each of which is distributed through the plate thickness, are investigated. The mechanical properties of the closed-cell layers are used to define the variation of Poisson's ratio and the relationship between the porosity coefficients and the mass density. For the GPL reinforced layer, the effective Young's modulus is derived with the Halpin-Tsai micro-system model, and the rule of mixtures is used to calculate the effective mass density and Poisson's ratio. The material of the upper 2D-FG layer is graded in two directions, and its effective mechanical properties are also derived with the rule of mixtures. The dynamic governing equations are derived with a first-order shear deformation theory (FSDT) and the von Kármán nonlinear theory. A combination of the dynamic relaxation (DR) and Newmark's direct integration methods is used to solve the governing equations in both time and space. A parametric study is carried out to explore the effects of the porosity coefficients, porosity and GPL distributions, material gradients, damping ratios, boundary conditions, and elastic foundation stiffnesses on the plate response. It is shown that both the distributions of the porosity and graphene nanofillers significantly affect the dynamic behaviors of the plates. It is also shown that the reduction in the dynamic deflection of the bilayer composite plates is maximized when the porosity and GPL distributions are symmetric.

Key words moving laminated plate, bidirectional functionally graded material (FGM), graphene nanoplatelet, porosity, first-order shear deformation theory (FSDT), Newmark's integration method

Chinese Library Classification O343.5

* Citation: ESMAEILZADEH, M., KADKHODAYAN, M., MOHAMMADI, S., and TURVEY, G. J. Nonlinear dynamic analysis of moving bilayer plates resting on elastic foundations. *Applied Mathematics and Mechanics* (*English Edition*) (2020) https://doi.org/10.1007/s10483-020-2587-8

† Corresponding author, E-mail: kadkhoda@um.ac.ir

2010 Mathematics Subject Classification 74A05, 74B20, 74E30, 74D10, 74H15, 74S20

1 Introduction

Due to the combined advantages of high stiffness and low self-weight, laminated composite plates are widely used in the aerospace, automotive, marine, and nuclear industries[1]. A laminated plate is an assembly of two or more layers (composed of fibres in a matrix material) which can be stacked to achieve the required mechanical properties such as high flexural stiffness, low thermal and electrical conductivity[2–4]. In the present investigation, the focus is on the dynamic response of a bilayer plate comprised of a bidirectional functionally graded (FG) layer and a graphene platelet (GPL) reinforced porous layer.

The foam is an engineering material which provides advantages such as low density, hardness and energy absorption capability. Recent reviews of foams[5–7] consider both random and uniform porosity distributions. Required mechanical properties have been used as design criteria for determining the size and distribution of the foams' internal cavities/pores in one or more directions, resulting in new porous structures[8]. Several theoretical methods have been proposed to predict the structural performance of FG porous beams. Gao et al.[9] used a Chebyshev surrogate model along with a discrete singular convolution technique to obtain dynamic performances of beams with different types of porosities. Based on an Euler-Bernoulli theory, the dynamic buckling behaviors of a simply-supported FG porous beam were also studied by Gao et al.[10]. Chen et al.[11–12] analyzed the elastic buckling, static flexure and free/forced vibration of beams made of porous graphite grains and open-cell metal foams, accounting for non-uniform distributions of the pores. Chen et al.[13] examined the effect of porosity on the nonlinear free vibration of sandwich beams with porous FG cores. The principal disadvantage of foam is the presence of internal cavities which reduce the structural stiffness and limit their engineering applications. However, stiffeners such as graphene and/or carbon nanotubes may be included in the foam to enhance its mechanical properties without adversely affecting its low self-weight. Porous nanocomposites can also lead to new applications in smart materials and other advanced technologies, e.g., fuel cells[14–15]. Most studies on nanocomposites focus on the mechanical properties and behaviors of structures reinforced with carbon nanotubes. Ansari and Torabi[16] undertook a numerical analysis of the vibration and buckling response of FG composite conical shells reinforced with carbon nanotubes. It has been demonstrated that the use of graphene nanoparticles is more advantageous than carbon nanotubes. A small quantity of graphene (as well as its derivatives) added to a polymer can significantly improve the composite material's mechanical properties. Rafiee et al.[17] showed that adding 0.1% of graphene nanoparticles to an epoxy matrix increases its Young's modulus by 31%, whereas only a 3 % increase is achieved by adding carbon nanotubes. Although it appears that graphene nanotubes provide the superior performance compared with carbon nanotubes in composite materials, it should be appreciated that graphene nanotube research is still in its early stage.

Yang et al.[18] analyzed multi-layer nanocomposite beams in which the graphene nanoparticles were distributed in the thickness direction. Their study showed that graphene nanoparticles significantly improved the buckling and post buckling behaviors of GPL-reinforced composite beams. Furthermore, it is suggested that this is sensitive to the distributions of the graphene nanoparticles (platelets). Wu et al.[19] and Song et al.[20] showed that, by combining 0.1% of graphene nanoparticles (in a non-uniform way) in a polymer matrix, a significant improvement was achieved. By means of the differential quadrature method, Gao et al.[21] performed a study on the free vibration of GPL-reinforced nanocomposite plates with closed-cell geometrical imperfections. Kitipornchai et al.[22] also investigated the nonlinear free vibration and elastic buckling response of porous nanocomposite beams reinforced with graphene. The effects of damping ratios on mechanical characteristics of FG porous shells with cylindrical shapes were investigated[23].

Functionally graded materials (FGMs) are relatively new composite materials in which the mechanical properties vary continuously and smoothly in one or more directions. The dynamic response of FG structures is an interesting and important subject which has attracted the attention of many researchers recently. By employing Hamilton's principle and Dannell theory, Gao et al.[24] investigated the nonlinear dynamic behavior of a cylindrical shell made of the materials which changed continuously through the shell thickness. Sofiyev and Kuruoglu[25] used the first-order shear deformation theory (FSDT) to study the vibration of simply-supported cylindrical sandwich shells with an FG core subject to static and time-dependent periodic axial forces and taking account of uniform and periodic FG distributions in the shell core. Nguyen et al.[26] also analyzed the nonlinear vibration of bidirectional FG Timoshenko beams under moving loads. Using a new third-order shear deformation theory, Lei et al.[27] explored the buckling behaviors of bidirectional FG beams with initial deflections.

Mobile structures are used in many engineering applications, e.g., train's carriages, aircraft's wings, marine vessels and moving walkways. Relevant to such applications, Esmaeilzadeh and Kadkhodayan[28] investigated the nonlinear dynamic deflection of a moving porous plate with the dynamic relaxation (DR) technique. The interaction of a fluid with a moving FG plate containing micro-voids was studied numerically by Wang and Yang[29]. Li et al.[30] reported a detailed study of the nonlinear forced vibration of an axially moving viscoelastic sandwich beam. Recently, the dynamic instability of an axially mobile viscoelastic plate subject to various boundary conditions was investigated by Zhou and Wang[31].

The computational models of structures resting on elastic media are commonly used to designate several real samples in industrial divisions. In many cases, elastic foundations can be considered as simple instruments such as springs. Takabatake[32] used a rectangular large floating plate located on elastic foundations with a variable spring stiffness to model a floating international airport. Gao et al.[33] showed the effects of some parameters such as damping ratios and temperature variations on the dynamic behaviors of a composite orthotropic plate resting on elastic foundations.

The present study is concerned with analyzing the dynamic behaviors of 2D FG/GPL plates resting on elastic foundations. Two nonlinear porosity distributions and three graphene distributions are analyzed, and the results are compared and contrasted. The analysis uses the DR and Newmark's methods to solve the governing equations. It appears that this is the first investigation of its type and the results may be of benefit to other researchers' future investigations.

2 Mechanical properties of the bilayer composite plate

Figure 1 shows a bilayer 2D FG/GPL-reinforced plate of thickness h ($h_{\mathrm{FGM}} + h_{\mathrm{GPL}}$), width

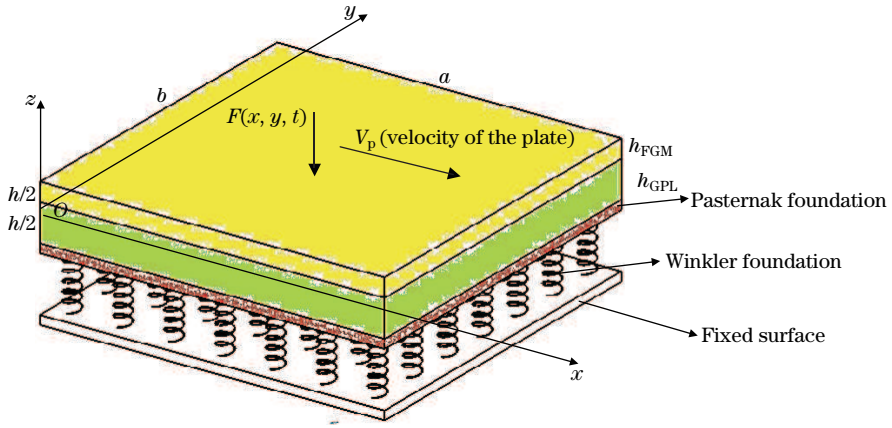

Fig. 1 A supported laminated rectangular plate with two layers through its thickness (color online)

b (the y-direction), and length a (the x-direction) in a Cartesian coordinate system. This plate travels along the x-direction with the constant speed of $V_{\rm p}$ and also is subject to a distributed impact load $F(x, y, t)$.

2.1 Bidirectional FG plates

The upper layer of the laminated plate is supposed to be made of two different elements whose mechanical properties change smoothly not only from the bottom ($z = h/2 - h_{\rm FGM}$) to the top ($z = h/2$), but also along the x-direction as shown in Fig. 2. In accordance with the rule of mixtures[34], the mechanical properties of the 2D FGM plate (Young's modulus E, Poisson's ratio υ, and density ρ) can be calculated as follows[27]:

$$\begin{cases} E_{\rm FGM}(x,z) = E_1 + (E_2 - E_1)\Big(\dfrac{z'}{h_{\rm FGM}}\Big)^n \Big(\dfrac{x}{a}\Big)^m, \\ \upsilon_{\rm FGM}(x,z) = \upsilon_1 + (\upsilon_2 - \upsilon_1)\Big(\dfrac{z'}{h_{\rm FGM}}\Big)^n \Big(\dfrac{x}{a}\Big)^m, \\ \rho_{\rm FGM}(x,z) = \rho_1 + (\rho_2 - \rho_1)\Big(\dfrac{z'}{h_{\rm FGM}}\Big)^n \Big(\dfrac{x}{a}\Big)^m, \\ z' = z + h_{\rm FGM} - \dfrac{h}{2}, \end{cases} \tag{1}$$

where the subscripts 1 and 2 denote the materials 1 and 2, respectively, and n and m are non-negative values that control material variations in the z- and x-directions, respectively. As depicted in Fig. 2, the composition of the 2D FG layer varies through the thickness direction from 100 % of the material 1 at the lower surface, $z = h/2 - h_{\rm FGM}$, to a mixture of the materials 1 and 2 at the top surface, $z = h/2$. The structure of the 2D FG layer also changes along the x-direction, from 100 % of the material 1 at $x = 0$, $z = h/2$ to 100 % of the material 2 at $x = a$, $z = h/2$.

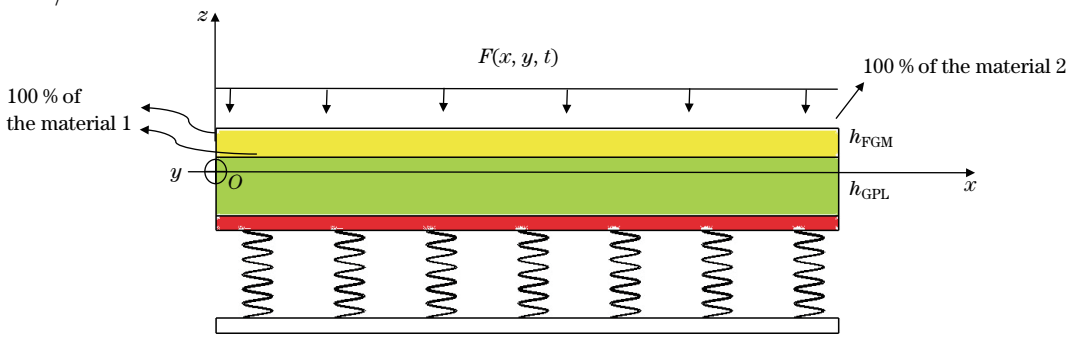

Fig. 2 Edge view of a laminated rectangular plate embedded on elastic foundations (color online)

2.2 Porosity and graphene distributions

Figure 2 illustrates a porous GPL-reinforced layer (foam) located under a 2D FGM layer ($-h/2 < z < -h/2 + h_{\rm GPL} (= h/2 - h_{\rm FGM})$). The two porosity distributions are shown in Fig. 3. The elastic and shear moduli and the porous nanocomposite layer's mass density with symmetric and unsymmetric porosity distributions 1 and 2 are[35]

$$\begin{cases} E(z) = E_{\rm c}\left(1 - \widehat{e}\lambda(z)\right), \\ G(z) = E(z)/\left(2(1+\upsilon(z))\right), \\ \rho(z) = \rho_{\rm c}\left(1 - e_{\rm m}\lambda(z)\right), \end{cases} \tag{2}$$

where

$$\lambda(z) = \begin{cases} \cos(\pi\overline{z}/h_{\rm GPL}) & \text{for the porosity distribution 1,} \\ \cos(\pi\overline{z}/(2h_{\rm GPL}) + \pi/4) & \text{for the porosity distribution 2,} \end{cases} \tag{3}$$

in which E_{c} and ρ_{c} are the maximum values of Young's modulus and the mass density of the nanocomposite layer without porosity[36], respectively, and $\overline{z} = z + \frac{h-h_{\mathrm{GPL}}}{2}$. The porosity coefficient $\widehat{e}$ can be obtained as

$$\widehat{e} = 1 - E_{\mathrm{d}}/E_{\mathrm{c}}. \tag{4}$$

Here, E_{d} is the minimum value of Young's modulus. Based on closed-cell patterns, the coefficient of mass density e_{m} using the Gaussian random field (GRF) model can be defined as follows[37]:

$$e_{\mathrm{m}} = \frac{1.121(1-(1-\widehat{e}\lambda(z))^{1/2.3})}{\lambda(z)}. \tag{5}$$

Also, according to the closed-cell GRF scheme, Poisson's ratio $\upsilon(z)$ can be obtained as[35]

$$\upsilon(z) = 0.342\upsilon_{\mathrm{c}}\Big(\frac{\rho(z)}{\rho_{\mathrm{c}}}\Big)^2 + (0.526\upsilon_{\mathrm{c}} - 0.221)\frac{\rho(z)}{\rho_{\mathrm{c}}} + 0.132\upsilon_{\mathrm{c}} + 0.221, \tag{6}$$

where υ_{c} indicates Poisson's ratio of pure matrix materials with no porosity.

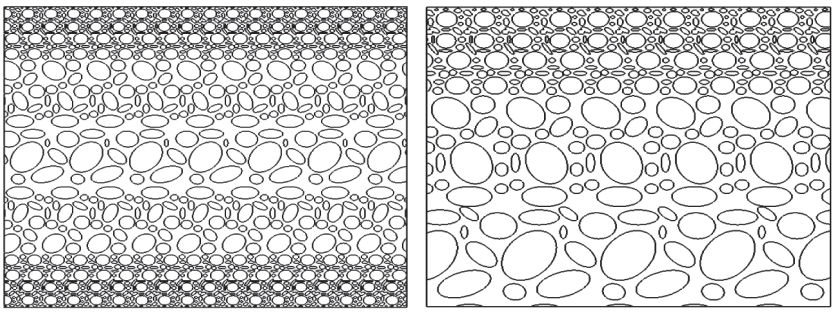

Fig. 3 Porosity distributions

The Halpin-Tsai micro-mechanics model[38] is used to calculate Young's modulus of the void-free nanocomposite. It is assumed that GPLs are randomly distributed in a matrix as rectangular solid fillers, the effective composite Young's modulus E_{c} is approximated as[35]

$$E_{\mathrm{c}} = \frac{3}{8}\Big(\frac{1+\chi_l^{\mathrm{GPL}}\omega_l^{\mathrm{GPL}}V_{\mathrm{GPL}}}{1-\omega_l^{\mathrm{GPL}}V_{\mathrm{GPL}}}\Big)E_{\mathrm{M}} + \frac{5}{8}\Big(\frac{1+\chi_w^{\mathrm{GPL}}\omega_w^{\mathrm{GPL}}V_{\mathrm{GPL}}}{1-\omega_w^{\mathrm{GPL}}V_{\mathrm{GPL}}}\Big)E_{\mathrm{M}}, \tag{7}$$

in which the filler geometry factors χ_l^{GPL} and χ_w^{GPL} for GPLs and the parameters ω_l^{GPL} and ω_w^{GPL} are

$$\begin{cases} \chi_l^{\mathrm{GPL}} = \dfrac{2l_{\mathrm{GPL}}}{t_{\mathrm{GPL}}}, \quad \chi_w^{\mathrm{GPL}} = \dfrac{2w_{\mathrm{GPL}}}{t_{\mathrm{GPL}}}, \\ \omega_l^{\mathrm{GPL}} = \dfrac{(E_{\mathrm{GPL}}/E_{\mathrm{M}})-1}{(E_{\mathrm{GPL}}/E_{\mathrm{M}})+\chi_l^{\mathrm{GPL}}}, \quad \omega_w^{\mathrm{GPL}} = \dfrac{(E_{\mathrm{GPL}}/E_{\mathrm{M}})-1}{(E_{\mathrm{GPL}}/E_{\mathrm{M}})+\chi_w^{\mathrm{GPL}}}, \end{cases} \tag{8}$$

where w_{GPL}, l_{GPL}, and t_{GPL} denote the average width, length, and thickness of GPLs, respectively, and E_{M} and E_{GPL} are Young's moduli of the metallic matrix and GPLs, respectively. The mass density ρ_{c} and Poisson's ratio υ_{c} of the GPL-reinforced metallic matrix can be calculated by using the rule of mixtures,

$$\begin{cases} \rho_{\mathrm{c}} = \rho_{\mathrm{GPL}}V_{\mathrm{GPL}} + \rho_{\mathrm{M}}V_{\mathrm{M}}, \\ \upsilon_{\mathrm{c}} = \upsilon_{\mathrm{GPL}}V_{\mathrm{GPL}} + \upsilon_{\mathrm{M}}V_{\mathrm{M}}, \end{cases} \tag{9}$$

where ρ_{GPL}, υ_{GPL}, and V_{GPL} (ρ_{M}, υ_{M}, and $V_{\mathrm{M}}=1-V_{\mathrm{GPL}}$) are the mass density, Poisson's ratio, and the volume fraction of GPLs (metallic matrix), respectively[22].

Based on the distributions in Fig. 4, namely, the patterns A, B, and C, the volume factors of GPLs can be written as follows[22]:

$$V_{\mathrm{GPL}}=\begin{cases} z_{i1}\left(1-\cos(\pi\beta(z))\right) & \text{for the pattern A,}\\ z_{i2}\Big(1-\cos\Big(\dfrac{\pi}{2}\beta(z)+\dfrac{\pi}{4}\Big)\Big) & \text{for the pattern B,}\\ z_{i3} & \text{for the pattern C,}\end{cases} \tag{10}$$

where $\beta(z)=\overline{z}/h_{\mathrm{GPL}}$. The maximum values of z_{i1}, z_{i2}, and z_{i3} can be calculated based on the weighting coefficient $\widehat{A}$ for the entire layer with the following equations[22]:

$$\begin{aligned}&\frac{\widehat{A}\rho_{\mathrm{M}}}{\widehat{A}\left(\rho_{\mathrm{M}}-\rho_{\mathrm{GPL}}\right)+\rho_{\mathrm{GPL}}}\int_{-h/2}^{-h/2+h_{\mathrm{GPL}}}\frac{\rho(z)}{\rho_{\mathrm{c}}}\mathrm{d}z\\ &=\begin{cases} z_{i1}\displaystyle\int_{-h/2}^{-h/2+h_{\mathrm{GPL}}}\left(1-\cos(\pi\beta(z))\right)\frac{\rho(z)}{\rho_{\mathrm{c}}}\mathrm{d}z & \text{for the pattern A,}\\ z_{i2}\displaystyle\int_{-h/2}^{-h/2+h_{\mathrm{GPL}}}\Big(1-\cos\Big(\frac{\pi}{2}\beta(z)+\frac{\pi}{4}\Big)\Big)\frac{\rho(z)}{\rho_{\mathrm{c}}}\mathrm{d}z & \text{for the pattern B,}\\ z_{i3}\displaystyle\int_{-h/2}^{-h/2+h_{\mathrm{GPL}}}\frac{\rho(z)}{\rho_{\mathrm{c}}}\mathrm{d}z & \text{for the pattern C.}\end{cases}\end{aligned} \tag{11}$$

It should be noted that $\rho(z)$ in these equations is related to the specific porosity distribution given in Eqs. (2) and (3).

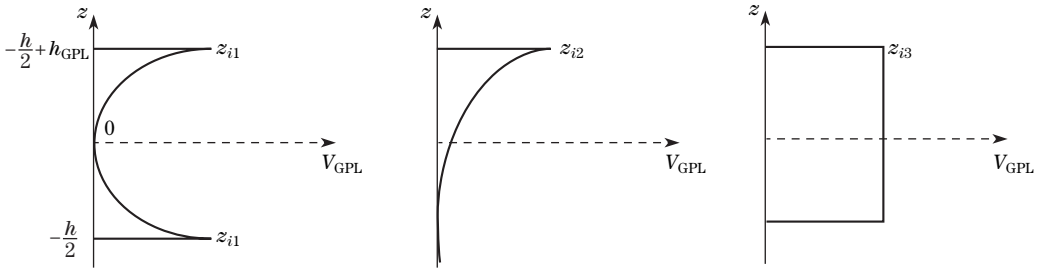

(a) Pattern A (b) Pattern B (c) Pattern C

Fig. 4 Three types of GPL distributions

2.3 Fundamental equations

To derive the governing equations, it is supposed that the layers are entirely interconnected, and hence there is no slippage at the interface between the layers of the plate. On the basis of the FSDT, the displacement fields are as follows:

$$\begin{cases} u_1(x,y,z,t)=u(x,y,t)+z\theta_x(x,y,t),\\ u_2(x,y,z,t)=v(x,y,t)+z\theta_y(x,y,t),\\ u_3(x,y,z,t)=w(x,y,t),\end{cases} \tag{12}$$

where u, v, and w are the displacement components of the middle surface in the directions of x, y, and z. Also, θ_x and θ_y are the rotational displacements about the y- and x-axes, respectively. In accordance with Hooke's law, the stress-strain relationships for bidimensional

FG and nanocomposite materials can be written as

$$\begin{pmatrix}\sigma_{xx}\\ \sigma_{yy}\\ \sigma_{xy}\\ \sigma_{yz}\\ \sigma_{xz}\end{pmatrix}_{\text{2D-FGM}} = \begin{pmatrix} Q_{11} & Q_{12} & 0 & 0 & 0\\ Q_{12} & Q_{11} & 0 & 0 & 0\\ 0 & 0 & Q_{66} & 0 & 0\\ 0 & 0 & 0 & C_{44} & 0\\ 0 & 0 & 0 & 0 & C_{55}\end{pmatrix}_{\text{2D-FGM}} \cdot (\boldsymbol{Y}_1 + z\boldsymbol{Y}_2)\,, \tag{13}$$

$$\begin{pmatrix}\sigma_{xx}\\ \sigma_{yy}\\ \sigma_{xy}\\ \sigma_{yz}\\ \sigma_{xz}\end{pmatrix}_{\text{GPL}} = \begin{pmatrix} A_{11} & A_{12} & 0 & 0 & 0\\ A_{12} & A_{11} & 0 & 0 & 0\\ 0 & 0 & A_{66} & 0 & 0\\ 0 & 0 & 0 & H_{44} & 0\\ 0 & 0 & 0 & 0 & H_{55}\end{pmatrix}_{\text{GPL}} \cdot (\boldsymbol{Y}_1 + z\boldsymbol{Y}_2)\,, \tag{14}$$

in which

$$\boldsymbol{Y}_1 = \begin{pmatrix} \dfrac{\partial u}{\partial x} + \dfrac{1}{2}\Big(\dfrac{\partial w}{\partial x}\Big)^2\\ \dfrac{\partial v}{\partial y} + \dfrac{1}{2}\Big(\dfrac{\partial w}{\partial y}\Big)^2\\ \dfrac{\partial u}{\partial y} + \dfrac{\partial v}{\partial x} + \dfrac{\partial w}{\partial x}\dfrac{\partial w}{\partial y}\\ \theta_y + \dfrac{\partial w}{\partial y}\\ \theta_x + \dfrac{\partial w}{\partial x}\end{pmatrix}, \quad \boldsymbol{Y}_2 = \begin{pmatrix} \dfrac{\partial \theta_x}{\partial x}\\ \dfrac{\partial \theta_y}{\partial y}\\ \dfrac{\partial \theta_x}{\partial y} + \dfrac{\partial \theta_y}{\partial x}\\ 0\\ 0\end{pmatrix},$$

$$\begin{cases} Q_{11} = \dfrac{E_{\text{FGM}}(x,z)}{1-\upsilon^2_{\text{FGM}}(x,z)} \quad \text{for the 2D FGM,}\\ Q_{12} = \dfrac{\upsilon_{\text{FGM}}(x,z)E_{\text{FGM}}(x,z)}{1-\upsilon^2_{\text{FGM}}(x,z)} \quad \text{for the 2D FGM,}\\ C_{44} = C_{55} = Q_{66} = G_{\text{FGM}}(x,z) = \dfrac{E_{\text{FGM}}(x,z)}{2(1+\upsilon_{\text{FGM}}(x,z))} \quad \text{for the 2D FGM,}\end{cases} \tag{15}$$

$$\begin{cases} A_{11} = \dfrac{E_{\text{GPL}}(z)}{1-\upsilon^2_{\text{GPL}}(z)} \quad \text{for the GPL,}\\ A_{12} = \dfrac{\upsilon_{\text{GPL}}(z)E_{\text{GPL}}(z)}{1-\upsilon^2_{\text{GPL}}(z)} \quad \text{for the GPL,}\\ H_{44} = H_{55} = A_{66} = G_{\text{GPL}}(z) = \dfrac{E_{\text{GPL}}(z)}{2(1+\upsilon_{\text{GPL}}(z))} \quad \text{for the GPL.}\end{cases} \tag{16}$$

Hamilton's principle is used in order to determine the fundamental equations of plates[24],

$$\int_0^T (\delta S + \delta X + \delta C - \delta P)\mathrm{d}t = 0, \tag{17}$$

where S signifies the strain energy of the structure, X is the virtual work done by the applied force, C denotes the potential energy of non-conservative forces resulting from damping effects, and P is the kinetic energy of the system. The symbol δ represents the variation operator. To obtain the variation of strain energy, the following equation is used:

$$\delta S = \iiint \sigma_{ij}\delta\varepsilon_{ij}\mathrm{d}V. \tag{18}$$

The virtual variation of potential energy of non-conservative forces resulting from damping influence is stated as below[24],

$$\delta C = \iiint C_{\mathrm{d}} \left(\rho(z) + \rho_{\mathrm{GPL}}(x,z)\right) \left(\dot{u}_1 \delta u_1 + \dot{u}_2 \delta u_2 + \dot{u}_3 \delta u_3\right) \mathrm{d}V. \tag{19}$$

Here, C_{d} is the corresponding symbol of the damping coefficient of the solid. The changes of virtual kinetic energy are obtained from the following equation:

$$\delta P = \iiint \left(\rho(z) + \rho_{\mathrm{GPL}}(x,z)\right) \left(\dot{u}_1 \delta \dot{u}_1 + \dot{u}_2 \delta \dot{u}_2 + \dot{u}_3 \delta \dot{u}_3\right) \mathrm{d}V. \tag{20}$$

The velocity vector of the axially moving plate can be obtained as[28]

$$\boldsymbol{V} = \Big(V_{\mathrm{p}} + \frac{\partial u_1}{\partial t} + V_{\mathrm{p}} \frac{\partial u_1}{\partial x}\Big)\boldsymbol{i} + \Big(\frac{\partial u_2}{\partial t} + V_{\mathrm{p}} \frac{\partial u_2}{\partial x}\Big)\boldsymbol{j} + \Big(\frac{\partial u_3}{\partial t} + V_{\mathrm{p}} \frac{\partial u_3}{\partial x}\Big)\boldsymbol{k}, \tag{21}$$

in which V_{p} is the velocity term, and $\boldsymbol{i}$, $\boldsymbol{j}$, and $\boldsymbol{k}$ are the unit vectors in the x-, y-, and z-axes of a three-dimensional (3D) Cartesian coordinate system, respectively. Hence, the variation of non-conservative forces of the system with consideration of Eq. (12) can be measured by

$$\begin{aligned}\delta C = \iiint C_{\mathrm{d}} \left(\rho(z) + \rho_{\mathrm{FGM}}(x,z)\right) \cdot \Big(\Big(V_{\mathrm{p}} + \frac{\partial(u + z\theta_x)}{\partial t} + V_{\mathrm{p}} \frac{\partial(u + z\theta_x)}{\partial x}\Big)\delta(u + z\theta_x) \\ + \Big(\frac{\partial(v + z\theta_y)}{\partial t} + V_{\mathrm{p}} \frac{\partial(v + z\theta_y)}{\partial x}\Big)\delta(v + z\theta_y) + \Big(\frac{\partial w}{\partial t} + V_{\mathrm{p}} \frac{\partial w}{\partial x}\Big)\delta w\Big)\mathrm{d}V.\end{aligned} \tag{22}$$

Similarly, the modified equation for the virtual kinetic energy is calculated as

$$\begin{aligned}\delta P = \iiint \left(\rho(z) + \rho_{\mathrm{FGM}}(x,z)\right) \cdot \Big(\Big(V_{\mathrm{p}} + \frac{\partial(u + z\theta_x)}{\partial t} + V_{\mathrm{p}} \frac{\partial(u + z\theta_x)}{\partial x}\Big) \\ \cdot \Big(\delta V_{\mathrm{p}} + \delta \frac{\partial(u + z\theta_x)}{\partial t} + V_{\mathrm{p}} \delta \frac{\partial(u + z\theta_x)}{\partial x}\Big) + \Big(\frac{\partial(v + z\theta_y)}{\partial t} + V_{\mathrm{p}} \frac{\partial(v + z\theta_y)}{\partial x}\Big) \\ \cdot \Big(\delta \frac{\partial(v + z\theta_y)}{\partial t} + V_{\mathrm{p}} \delta \frac{\partial(v + z\theta_y)}{\partial x}\Big) + \Big(\frac{\partial w}{\partial t} + V_{\mathrm{p}} \frac{\partial w}{\partial x}\Big)\Big(\delta \frac{\partial w}{\partial t} + V_{\mathrm{p}} \delta \frac{\partial w}{\partial x}\Big)\Big)\mathrm{d}V.\end{aligned} \tag{23}$$

Figure 1 reveals that $-\frac{h}{2} + h_{\mathrm{GPL}}$ and $\frac{h}{2} - h_{\mathrm{FGM}}$ are equal. Therefore, the inertia of the whole body can be obtained as

$$I_k = \int_{-h/2}^{h/2-h_{\mathrm{FGM}}} \rho(z) z^k \mathrm{d}z + \int_{h/2-h_{\mathrm{FGM}}}^{h/2} \rho_{\mathrm{FGM}}(x,z) z^k \mathrm{d}z, \quad k = 0, 1, 2. \tag{24}$$

The principal equations of a nanocomposite plate subject to a dynamic load $F(x,y,t)$ are based on Hamilton's theory as follows[39]:

$$\begin{cases} \dfrac{\partial N_{xx}}{\partial x} + \dfrac{\partial N_{xy}}{\partial y} = I_0\Big(\dfrac{\mathrm{D}^2 u}{\mathrm{D}t^2} + C_{\mathrm{d}} V_{\mathrm{p}} + C_{\mathrm{d}} \dfrac{\mathrm{D}u}{\mathrm{D}t}\Big) + I_1\Big(\dfrac{\mathrm{D}^2 \theta_x}{\mathrm{D}t^2} + C_{\mathrm{d}} \dfrac{\mathrm{D}\theta_x}{\mathrm{D}t}\Big), \\ \dfrac{\partial N_{xy}}{\partial x} + \dfrac{\partial N_{yy}}{\partial y} = I_0\Big(\dfrac{\mathrm{D}^2 v}{\mathrm{D}t^2} + C_{\mathrm{d}} \dfrac{\mathrm{D}v}{\mathrm{D}t}\Big) + I_1\Big(\dfrac{\mathrm{D}^2 \theta_y}{\mathrm{D}t^2} + C_{\mathrm{d}} \dfrac{\mathrm{D}\theta_y}{\mathrm{D}t}\Big), \\ \dfrac{\partial Q_x}{\partial x} + \dfrac{\partial Q_y}{\partial y} + N(w) + F(x,y,t) - K_{\mathrm{w}} w + K_{\mathrm{s}}\Big(\dfrac{\partial^2 w}{\partial x^2} + \dfrac{\partial^2 w}{\partial y^2}\Big) = I_0\Big(\dfrac{\mathrm{D}^2 w}{\mathrm{D}t^2} + C_{\mathrm{d}} \dfrac{\mathrm{D}w}{\mathrm{D}t}\Big), \\ \dfrac{\partial M_{xx}}{\partial x} + \dfrac{\partial M_{xy}}{\partial y} - Q_x = I_1\Big(\dfrac{\mathrm{D}^2 u}{\mathrm{D}t^2} + C_{\mathrm{d}} V_{\mathrm{p}} + C_{\mathrm{d}} \dfrac{\mathrm{D}u}{\mathrm{D}t}\Big) + I_2\Big(\dfrac{\mathrm{D}^2 \theta_x}{\mathrm{D}t^2} + C_{\mathrm{d}} \dfrac{\mathrm{D}\theta_x}{\mathrm{D}t}\Big), \\ \dfrac{\partial M_{xy}}{\partial x} + \dfrac{\partial M_{yy}}{\partial y} - Q_y = I_1\Big(\dfrac{\mathrm{D}^2 v}{\mathrm{D}t^2} + C_{\mathrm{d}} \dfrac{\mathrm{D}v}{\mathrm{D}t}\Big) + I_2\Big(\dfrac{\mathrm{D}^2 \theta_y}{\mathrm{D}t^2} + C_{\mathrm{d}} \dfrac{\mathrm{D}\theta_y}{\mathrm{D}t}\Big), \end{cases} \tag{25}$$

in which

$$N(w)=N_{xx}\frac{\partial^2 w}{\partial x^2}+2N_{xy}\frac{\partial^2 w}{\partial x\partial y}+N_{yy}\frac{\partial^2 w}{\partial y^2},$$
$$\begin{cases}\dfrac{\mathrm{D}^2}{\mathrm{D}t^2}=\dfrac{\partial^2}{\partial t^2}+2V_{\mathrm{p}}\dfrac{\partial^2}{\partial x\partial t}+V_{\mathrm{p}}^2\dfrac{\partial^2}{\partial x^2},\\ \dfrac{\mathrm{D}}{\mathrm{D}t}=\dfrac{\partial}{\partial t}+V_{\mathrm{p}}\dfrac{\partial}{\partial x},\end{cases}\tag{26}$$

K_{w} is the Winkler foundation modulus, and K_{s} is the Pasternak shear foundation. Also, the damping coefficient can be related to the damping ratio as

$$C_{\mathrm{d}}=2\xi\omega_{\mathrm{n}},\tag{27}$$

in which ξ and ω_{n} are, respectively, the damping ratio of the plate and the circular natural frequency. Similar to Eq. (24), the stress resultants are

$$\begin{cases}(N_i,M_i)=\displaystyle\int_{-h/2}^{h/2-h_{\mathrm{FGM}}}((1,z)\,\sigma_i)_{\mathrm{GPL}}\,\mathrm{d}z+\int_{h/2-h_{\mathrm{FGM}}}^{h/2}((1,z)\,\sigma_i)_{\mathrm{2D\text{-}FGM}}\,\mathrm{d}z,\quad i=xx,yy,xy,\\ Q_i=K^2\left(\displaystyle\int_{-h/2}^{h/2-h_{\mathrm{FGM}}}(\sigma_{iz})_{\mathrm{GPL}}\,\mathrm{d}z+\int_{h/2-h_{\mathrm{FGM}}}^{h/2}(\sigma_{iz})_{\mathrm{2D\text{-}FGM}}\,\mathrm{d}z\right),\quad i=x,y,\end{cases}\tag{28}$$

where K^2 is the transverse shear correction coefficient equal to 0.833. The boundary conditions used in the present study are as follows.

(i) The simply-supported boundary condition (SSSS)

$$\begin{cases}u=v=w=\theta_y=M_{xx}=0, & \text{when } x=0,a,\\ u=v=w=\theta_x=M_{yy}=0, & \text{when } y=0,b.\end{cases}\tag{29}$$

(ii) The clamped boundary condition (CCCC)

$$\begin{cases}u=v=w=\theta_x=\theta_y=0, & \text{when } x=0,a,\\ u=v=w=\theta_x=\theta_y=0, & \text{when } y=0,b.\end{cases}\tag{30}$$

3 Solution methodology of the nonlinear equations

In the current investigation, Newmark's method[28] is used to discretize Eq. (25) in the time domain, and then the viscous DR technique along with a finite difference discretization scheme is used to solve the differential equations.

3.1 Newmark's integration method

In Newmark's method, the real velocity and acceleration vectors at t_{j+1} (j is the number of time steps) are as follows:

$$\dot{\boldsymbol{x}}_{j+1}=\frac{\gamma}{\beta\Delta t_j}(\boldsymbol{x}_{\boldsymbol{j}+1}-\boldsymbol{x}_{\boldsymbol{j}})-\Big(\frac{\gamma}{\beta}-1\Big)\dot{\boldsymbol{x}}_{\boldsymbol{j}}-\Big(\frac{\gamma}{2\beta}-1\Big)\ddot{\boldsymbol{x}}_j\Delta t_j,\tag{31}$$

$$\ddot{\boldsymbol{x}}_{j+1}=\frac{1}{\beta(\Delta t_j)^2}(\boldsymbol{x}_{\boldsymbol{j}+1}-\boldsymbol{x}_{\boldsymbol{j}})-\frac{1}{\beta\Delta t_j}\dot{\boldsymbol{x}}_{\boldsymbol{j}}-\Big(\frac{1}{2\beta}-1\Big)\ddot{\boldsymbol{x}}_j,\tag{32}$$

in which γ and β are Newmark's constants and assumed to be 0.5 and 0.25 (constant average acceleration method), respectively, for obtaining stable and convergent results. Furthermore, $\boldsymbol{x}$ is the displacement field of the plate ($\boldsymbol{x}=\boldsymbol{u},\boldsymbol{v},\boldsymbol{w},\boldsymbol{\psi}_x,\boldsymbol{\psi}_y$), and Δt is the real time interval.

By substituting Eqs. (31) and (32) into Eq. (25), it becomes

$$
\begin{cases}
\dfrac{\partial N_{xx}}{\partial x}+\dfrac{\partial N_{xy}}{\partial y}-\Big(\Big(A_0+2V_{\mathrm{p}}B_0\dfrac{\partial}{\partial x}+V_{\mathrm{p}}^2\dfrac{\partial^2}{\partial x^2}+C_{\mathrm{d}}B_0\Big)(I_0\boldsymbol{u}_{j+1}+I_1\boldsymbol{\theta}_{x,j+1})\\
+C_{\mathrm{d}}\Big(I_0\Big(1+\dfrac{\partial \boldsymbol{u}_{j+1}}{\partial x}\Big)V_{\mathrm{p}}+I_1V_{\mathrm{p}}\dfrac{\partial \boldsymbol{\theta}_{x,j+1}}{\partial x}\Big)\Big)=-\Big(I_0\Big((A_0+C_{\mathrm{d}}B_0)\boldsymbol{u}_j+(A_1+C_{\mathrm{d}}B_1)\dot{\boldsymbol{u}}_j\\
+(A_2+C_{\mathrm{d}}B_2)\ddot{\boldsymbol{u}}_j+2V_{\mathrm{p}}\Big(B_0\dfrac{\partial \boldsymbol{u}_j}{\partial x}+B_1\dfrac{\partial \dot{\boldsymbol{u}}_j}{\partial x}+B_2\dfrac{\partial \ddot{\boldsymbol{u}}_j}{\partial x}\Big)\Big)+I_1\Big((A_0+C_{\mathrm{d}}B_0)\boldsymbol{\theta}_{x,j}\\
+(A_1+C_{\mathrm{d}}B_1)\dot{\boldsymbol{\theta}}_{x,j}+(A_2+C_{\mathrm{d}}B_2)\ddot{\boldsymbol{\theta}}_{x,j}+2V_{\mathrm{p}}\Big(B_0\dfrac{\partial \boldsymbol{\theta}_{x,j}}{\partial x}+B_1\dfrac{\partial \dot{\boldsymbol{\theta}}_{x,j}}{\partial x}+B_2\dfrac{\partial \ddot{\boldsymbol{\theta}}_{x,j}}{\partial x}\Big)\Big)\Big),\\
\dfrac{\partial N_{xy}}{\partial x}+\dfrac{\partial N_{yy}}{\partial y}-\Big(\Big(A_0+2V_{\mathrm{p}}B_0\dfrac{\partial}{\partial x}+V_{\mathrm{p}}^2\dfrac{\partial^2}{\partial x^2}+C_{\mathrm{d}}B_0\Big)(I_0\boldsymbol{v}_{j+1}+I_1\boldsymbol{\theta}_{y,j+1})\\
+C_{\mathrm{d}}\Big(I_0V_{\mathrm{p}}\dfrac{\partial \boldsymbol{v}_{j+1}}{\partial x}+I_1V_{\mathrm{p}}\dfrac{\partial \boldsymbol{\theta}_{y,j+1}}{\partial x}\Big)\Big)=-\Big(I_0\Big((A_0+C_{\mathrm{d}}B_0)\boldsymbol{v}_j+(A_1+C_{\mathrm{d}}B_1)\dot{\boldsymbol{v}}_j\\
+(A_2+C_{\mathrm{d}}B_2)\ddot{\boldsymbol{v}}_j+2V_{\mathrm{p}}\Big(B_0\dfrac{\partial \boldsymbol{v}_j}{\partial x}+B_1\dfrac{\partial \dot{\boldsymbol{v}}_j}{\partial x}+B_2\dfrac{\partial \ddot{\boldsymbol{v}}_j}{\partial x}\Big)\Big)+I_1\Big((A_0+C_{\mathrm{d}}B_0)\boldsymbol{\theta}_{y,j}\\
+(A_1+C_{\mathrm{d}}B_1)\dot{\boldsymbol{\theta}}_{y,j}+(A_2+C_{\mathrm{d}}B_2)\ddot{\boldsymbol{\theta}}_{y,j}+2V_{\mathrm{p}}\Big(B_0\dfrac{\partial \boldsymbol{\theta}_{y,j}}{\partial x}+B_1\dfrac{\partial \dot{\boldsymbol{\theta}}_{y,j}}{\partial x}+B_2\dfrac{\partial \ddot{\boldsymbol{\theta}}_{y,j}}{\partial x}\Big)\Big)\Big),
\end{cases}
\tag{33a}
$$

$$
\begin{cases}
\dfrac{\partial Q_x}{\partial x}+\dfrac{\partial Q_y}{\partial y}+N(w)-K_{\mathrm{w}}\boldsymbol{w}+K_{\mathrm{s}}\Big(\dfrac{\partial^2 \boldsymbol{w}}{\partial x^2}+\dfrac{\partial^2 \boldsymbol{w}}{\partial y^2}\Big)-\Big(\Big(A_0+2V_{\mathrm{p}}B_0\dfrac{\partial}{\partial x}+V_{\mathrm{p}}^2\dfrac{\partial^2}{\partial x^2}\\
+C_{\mathrm{d}}B_0\Big)I_0\boldsymbol{w}_{j+1}+C_{\mathrm{d}}\Big(I_0V_{\mathrm{p}}\dfrac{\partial \boldsymbol{w}_{j+1}}{\partial x}\Big)\Big)=-I_0\Big((A_0+C_{\mathrm{d}}B_0)\boldsymbol{w}_j+(A_1+C_{\mathrm{d}}B_1)\dot{\boldsymbol{w}}_j\\
+(A_2+C_{\mathrm{d}}B_2)\ddot{\boldsymbol{w}}_j+2V_{\mathrm{p}}\Big(B_0\dfrac{\partial \boldsymbol{w}_j}{\partial x}+B_1\dfrac{\partial \dot{\boldsymbol{w}}_j}{\partial x}+B_2\dfrac{\partial \ddot{\boldsymbol{w}}_j}{\partial x}\Big)\Big)-F(x,y,t),\\
\dfrac{\partial M_{xx}}{\partial x}+\dfrac{\partial M_{xy}}{\partial y}-Q_x-\Big(\Big(A_0+2V_{\mathrm{p}}B_0\dfrac{\partial}{\partial x}+V_{\mathrm{p}}^2\dfrac{\partial^2}{\partial x^2}+C_{\mathrm{d}}B_0\Big)(I_1\boldsymbol{u}_{j+1}+I_2\boldsymbol{\theta}_{x,j+1})\\
+C_{\mathrm{d}}\Big(I_1\Big(1+\dfrac{\partial \boldsymbol{u}_{j+1}}{\partial x}\Big)V_{\mathrm{p}}+I_2V_{\mathrm{p}}\dfrac{\partial \boldsymbol{\theta}_{x,j+1}}{\partial x}\Big)\Big)=-\Big(I_1\Big((A_0+C_{\mathrm{d}}B_0)\boldsymbol{u}_j\\
+(A_1+C_{\mathrm{d}}B_1)\dot{\boldsymbol{u}}_j+(A_2+C_{\mathrm{d}}B_2)\ddot{\boldsymbol{u}}_j+2V_{\mathrm{p}}\Big(B_0\dfrac{\partial \boldsymbol{u}_j}{\partial x}+B_1\dfrac{\partial \dot{\boldsymbol{u}}_j}{\partial x}+B_2\dfrac{\partial \ddot{\boldsymbol{u}}_j}{\partial x}\Big)\Big)\\
+I_2\Big((A_0+C_{\mathrm{d}}B_0)\boldsymbol{\theta}_{x,j}+(A_1+C_{\mathrm{d}}B_1)\dot{\boldsymbol{\theta}}_{x,j}+(A_2+C_{\mathrm{d}}B_2)\ddot{\boldsymbol{\theta}}_{x,j}\\
+2V_{\mathrm{p}}\Big(B_0\dfrac{\partial \boldsymbol{\theta}_{x,j}}{\partial x}+B_1\dfrac{\partial \dot{\boldsymbol{\theta}}_{x,j}}{\partial x}+B_2\dfrac{\partial \ddot{\boldsymbol{\theta}}_{x,j}}{\partial x}\Big)\Big)\Big),\\
\dfrac{\partial M_{xy}}{\partial x}+\dfrac{\partial M_{yy}}{\partial y}-Q_y-\Big(\Big(A_0+2V_{\mathrm{p}}B_0\dfrac{\partial}{\partial x}+V_{\mathrm{p}}^2\dfrac{\partial^2}{\partial x^2}+C_{\mathrm{d}}B_0\Big)(I_1\boldsymbol{v}_{j+1}+I_2\boldsymbol{\theta}_{y,j+1})\\
+C_{\mathrm{d}}(I_1V_{\mathrm{p}}\dfrac{\partial \boldsymbol{v}_{j+1}}{\partial x}+I_2V_{\mathrm{p}}\dfrac{\partial \boldsymbol{\theta}_{y,j+1}}{\partial x}\Big)\Big)=-\Big(I_1\Big((A_0+C_{\mathrm{d}}B_0)\boldsymbol{v}_j+(A_1+C_{\mathrm{d}}B_1)\dot{\boldsymbol{v}}_j\\
+(A_2+C_{\mathrm{d}}B_2)\ddot{\boldsymbol{v}}_j+2V_{\mathrm{p}}\Big(B_0\dfrac{\partial \boldsymbol{v}_j}{\partial x}+B_1\dfrac{\partial \dot{\boldsymbol{v}}_j}{\partial x}+B_2\dfrac{\partial \ddot{\boldsymbol{v}}_j}{\partial x}\Big)\Big)+I_2\Big((A_0+C_{\mathrm{d}}B_0)\boldsymbol{\theta}_{y,j}\\
+(A_1+C_{\mathrm{d}}B_1)\dot{\boldsymbol{\theta}}_{y,j}+(A_2+C_{\mathrm{d}}B_2)\ddot{\boldsymbol{\theta}}_{y,j}+2V_{\mathrm{p}}\Big(B_0\dfrac{\partial \boldsymbol{\theta}_{y,j}}{\partial x}+B_1\dfrac{\partial \dot{\boldsymbol{\theta}}_{y,j}}{\partial x}+B_2\dfrac{\partial \ddot{\boldsymbol{\theta}}_{y,j}}{\partial x}\Big)\Big)\Big),
\end{cases}
\tag{33b}
$$

in which

$$\begin{cases} A_0 = \dfrac{4}{(\Delta t_j)^2}, \quad A_1 = \dfrac{4}{\Delta t_j}, \quad A_2 = 1, \\ B_0 = \dfrac{2}{\Delta t_j}, \quad B_1 = 1, \quad B_2 = 0. \end{cases} \tag{34}$$

For the sake of briefness, Eq. (33) can be rewritten as

$$\overline{\boldsymbol{K}}_{j+1}\boldsymbol{x}_{j+1} = \overline{\boldsymbol{P}}_{j+1}, \tag{35}$$

where $\overline{\boldsymbol{K}}_{j+1}$ and $\overline{\boldsymbol{P}}_{j+1}$ are the equivalent stiffness matrix and vector, respectively.

3.2 DR method

Equation (30) is transformed to the fictitious dynamic space by adding the artificial mass and damping terms. This method is called the viscous DR[40],

$$\boldsymbol{M}^n_{\mathrm{DR}}\boldsymbol{a}^n + \boldsymbol{C}^n_{\mathrm{DR}}\boldsymbol{v}^n + \overline{\boldsymbol{K}}^n_{j+1}\boldsymbol{x}^n_{j+1} = \overline{\boldsymbol{P}}^n_{j+1}, \tag{36}$$

in which $\boldsymbol{M}^n_{\mathrm{DR}}$ and $\boldsymbol{C}^n_{\mathrm{DR}}$ are the diagonal fictitious mass and damping matrices in the nth DR iteration, respectively. Moreover, $\boldsymbol{v}$ and $\boldsymbol{a}$ are fictitious velocity and acceleration vectors, respectively. Here, artificial mass matrix elements and nodal damping factors, which control the stability of DR method, are estimated as follows[41]:

$$m^{D_{\mathrm{OF}}}_{ii} \geqslant 0.25(\tau^n)^2 \sum_{l=1}^{D_{\mathrm{OF}}} |k_{il}|, \quad \boldsymbol{K} = \frac{\partial(\overline{\boldsymbol{K}}^n_{j+1}\boldsymbol{x}^n_{j+1})}{\partial \boldsymbol{x}}, \tag{37}$$

$$c^n_i = 2\left(\frac{(\boldsymbol{x}^n)^{\mathrm{T}}\,\overline{\boldsymbol{P}}^n_{j+1,i}}{(\boldsymbol{x}^n)^{\mathrm{T}}\,m^n_{ii}\boldsymbol{x}^n}\right)^{1/2}, \tag{38}$$

in which D_{OF} denotes the number of degrees of freedom of the structure, it is 5 in the present study, the symbol n represents the nth iteration, k is the element of the stiffness matrix $\boldsymbol{K}$, m is the element of the diagonal matrix $\boldsymbol{M}$, c is the element of the diagonal matrix $\boldsymbol{C}$, and τ is an increment of fictitious time usually taken equal to 1. Moreover, $\boldsymbol{x} = \boldsymbol{u}, \boldsymbol{v}, \boldsymbol{w}, \boldsymbol{\psi}_x, \boldsymbol{\psi}_y$ is the approximate solution vector. To complete the iteration process, the velocity and acceleration terms are substituted by the following equivalent central finite-difference expressions:

$$\boldsymbol{v}^{n-(1/2)} = (\boldsymbol{x}^n - \boldsymbol{x}^{n-1})/\tau^n, \tag{39}$$

$$\boldsymbol{a}^n = (\boldsymbol{v}^{n+(1/2)} - \boldsymbol{v}^{n-(1/2)})/\tau^n. \tag{40}$$

By integrating velocities after each time step, the displacements can be obtained as[1]

$$\boldsymbol{x}^{n+1} = \boldsymbol{x}^n + \tau^{n+1}\boldsymbol{v}^{n+(1/2)}. \tag{41}$$

The dynamic relaxation process keeps running until the steady state situation happens (i.e., $\sum\limits_l v_l^{n+(1/2)} \leqslant 10^{-12}$ and $|\overline{\boldsymbol{P}}^n_{j+1} - \overline{\boldsymbol{K}}^n_{j+1}\boldsymbol{x}^n_{j+1}| \leqslant 10^{-9}$). These steps are iterated for each time increment of Newmark's method.

4 Numerical results and discussion

4.1 Validation

Example 1 There are no results for porous GPL/metal nanocomposite plates. The present analysis is applied to a simply-supported square non-porous epoxy plate reinforced with GPLs.

The geometric and material properties are

$$\begin{cases} a = b = 0.45 \text{ m}, \quad h = 0.045 \text{ m}, \\ l_{\text{GPL}} = 2.5 \text{ μm}, \quad w_{\text{GPL}} = 1.5 \text{ μm}, \quad t_{\text{GPL}} = 1.5 \text{ nm}, \\ E_{\text{GPL}} = 1.01 \text{ TPa}, \quad \rho_{\text{GPL}} = 1\,060 \text{ kg/m}^3, \quad \upsilon_{\text{GPL}} = 0.186, \\ E_{\text{M}} = 3.0 \text{ GPa}, \quad \rho_{\text{M}} = 1\,200 \text{ kg/m}^3, \quad \upsilon_{\text{M}} = 0.34. \end{cases} \tag{42}$$

For the dynamic analysis, the plate is subject to a triangular pressure pulse load which is uniformly distributed over the whole upper surface of the plate, but decays linearly over time (see Fig. 5) as

$$F(x, y, t) = \begin{cases} P_{\text{m}}(1 - t/T_{\text{P}}), & 0 \leqslant t \leqslant T_{\text{P}}, \\ 0, & t > T_{\text{P}}, \end{cases} \tag{43}$$

where P_{m} is the maximum pulse pressure, and T_{P} is the duration time of loading. The values of P_{m} and T_{P} are assumed to be 500 kPa and 0.01 s, respectively. To model graphene distributions inside the plate, Song et al.[20] utilized linear patterns as

$$\lambda(z) = \begin{cases} \dfrac{2\,|z|}{h} & \text{for the symmetric pattern,} \\ \dfrac{1}{2} + \dfrac{z}{h} & \text{for the unsymmetric pattern,} \\ 1 & \text{for the uniform pattern.} \end{cases} \tag{44}$$

As seen in Fig. 6, the results obtained are in good agreement with those reported in Ref. [20]. The results depict that the distribution of more GPLs near the top and bottom surfaces of the plates, where the stress is maximum, leads to a greater reduction of the dynamic responses of the plates. It also has to be mentioned that w_{c} is the maximum dynamic centre deflection of the GPL-reinforced plate, and w_{m} is the maximum value of transient deflection at the centre of the plate without GPLs, which is $0.63{\times}10^{-2}$ m at $t = 1.5 \times 10^{-3}$ s.

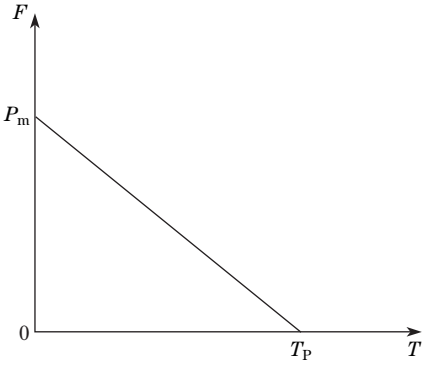

Fig. 5 A triangular pressure pulse load

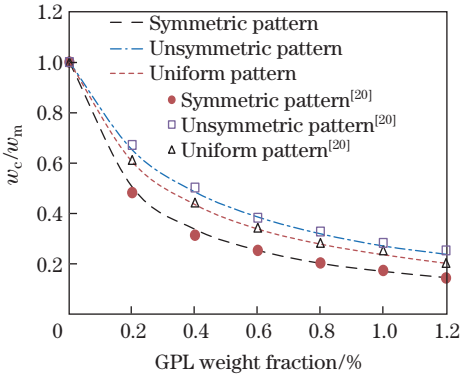

Fig. 6 Effects of GPL weight fractions on $w_{\text{c}}/w_{\text{m}}$ for simply-supported GPL/epoxy nanocomposite plates when $w_{\text{m}} = 0.63{\times}10^{-2}$ m (color online)

Example 2 The comparison of dimensionless transverse displacement $\left(= \frac{100 E_1 h^3 w_{\text{centre}}}{12 a^4 (1-\upsilon_1^2) F_0}\right)$ at the centre of the plate and axial stress $\left(= \frac{h^2}{F_0 a^2}\sigma_{xx}\right)$ for the FG square plate subject to a harmonic load $(F(x, y, t) = F_0 \sin(2\,000t), 0 < t \leqslant 8$ ms) for the CCCC boundary condition is

plotted in Figs. 7 and 8. The amplitude of applied load, geometrical dimensions and mechanical properties of the plate are given as

$$\begin{cases} F_0 = 1 \text{ MPa}, \quad a = b = 5 \times 10^{-2} \text{ m}, \quad h = 1 \times 10^{-2} \text{ m}, \\ E_1 = 70 \text{ GPa}, \quad \rho_1 = 2\,702 \text{ kg/m}^3, \quad \upsilon_1 = 0.3, \\ E_2 = 200 \text{ GPa}, \quad \rho_2 = 5\,700 \text{ kg/m}^3, \quad \upsilon_2 = 0.3. \end{cases} \tag{45}$$

From Figs. 7 and 8, it is noticed that the present numerical method predicts the dynamic deflection and stress very precisely compared with those in Ref. [42].

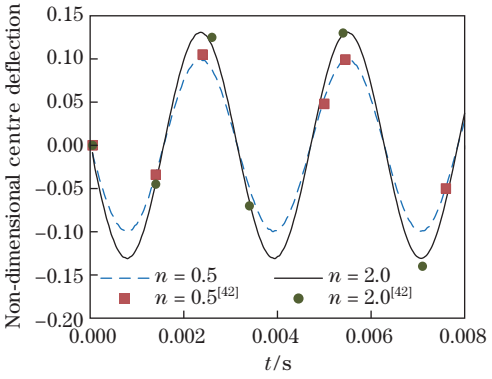

Fig. 7 Time history of the non-dimensional centre deflection of a clamped square FG plate (color online)

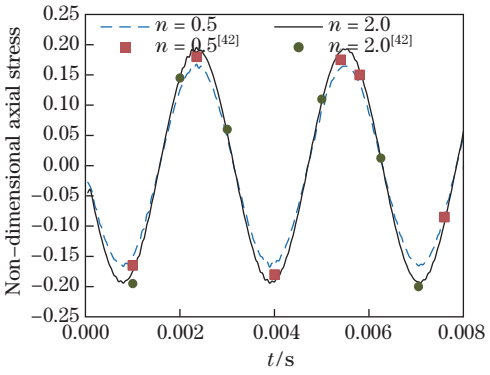

Fig. 8 Time history of the non-dimensional axial stress at the centre of the top surface of a clamped square FG plate (color online)

Example 3 In this example, the accuracy of the current model is confirmed by comparing the dynamic responses of a clamped beam moving with a constant dimensionless velocity, $U = 1$ with those found by An and Sue[43]. They utilized the following parameters to obtain the results:

$$\begin{cases} \dfrac{\partial^2 W}{\partial t^2} + 2U\dfrac{\partial^2 W}{\partial x \partial t} - (1 - U^2)\dfrac{\partial^2 W}{\partial x^2} + \dfrac{EI}{P_0 a^2}\dfrac{\partial^4 W}{\partial x^4} = 0, \\ W = \dfrac{w}{a}, \quad U = V_{\mathrm{p}}\sqrt{\dfrac{\rho}{P_0}}, \quad T = t\sqrt{\dfrac{P_0}{\rho a^2}}, \end{cases} \tag{46}$$

in which w, W, V_{p}, U, P_0, EI, ρ, and a represent the dimensional transverse centre displacement, the non-dimensional centre deflection, the dimensional velocity, the non-dimensional velocity, the axial tension, the flexural rigidity, the mass density of the structure, and its length, respectively. Moreover, t and T are, respectively, time and non-dimensional time. As seen from Fig. 9, it is evident that the DR-Newmark method is really effective for solving moving beam problems.

Example 4 Finally, the effects of two types of foundations on the deflection of a simply-supported GPL-reinforced nanocomposite with the side length of 0.9 m and the thickness of 0.045 m with $K_{\mathrm{w}} = 0.1$ GPa/m and $K_{\mathrm{s}} = 0.01$ GPa·m are investigated, and the results are compared with solutions in Ref. [44]. Figure 10 shows that the present results match well with those reported in Ref. [44].

4.2 Closed-cell solids on elastic foundations

In this part, the effects of the elastic foundations, porosity fractions, porosity, and GPL distributions on the dimensionless dynamic central deflection and the vibration of moving bilayer plates with closed-cell porosities are investigated.

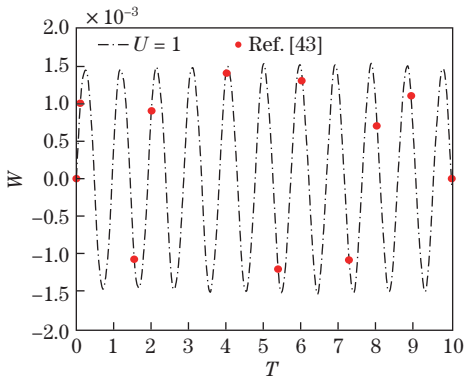

Fig. 9 Dimensionless centre deflections of a clamped moving beam at the dimensionless velocity of 1 when $\frac{EI}{P_0 a^2} = 0.1$ (color online)

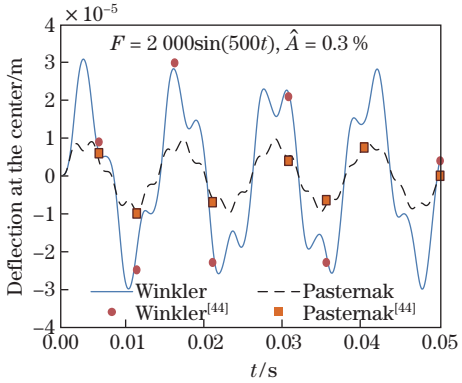

Fig. 10 Effects of elastic foundations on the central dynamic deflection of a simply-supported nanocomposite plate when $l_{\mathrm{GPL}} = 2.5$ μm, $w_{\mathrm{GPL}} = 1.5$ μm, and $t_{\mathrm{GPL}} = 15$ nm (color online)

Unless mentioned otherwise, the weight fraction of GPL, the velocity of the moving plate, and the values of material gradient indices n and m will be, respectively, 2 %, 5 m/s, 2 and 2. Also, the geometrical and material properties are as follows:

$$\begin{cases} a = b = 2 \text{ m}, \quad h = 0.15 \text{ m} \quad (h_{\mathrm{GPL}} = 0.1 \text{ m}, \quad h_{\mathrm{FGM}} = 0.05 \text{ m}), \\ l_{\mathrm{GPL}} = 6 \text{ μm}, \quad w_{\mathrm{GPL}} = 3 \text{ μm}, \quad t_{\mathrm{GPL}} = 3 \text{ nm}, \\ E_1 = 116 \text{ GPa}, \quad \upsilon_1 = 0.34, \quad \rho_1 = 1\,200 \text{ kg/m}^3, \\ E_2 = 380 \text{ GPa}, \quad \upsilon_2 = 0.34, \quad \rho_2 = 3\,960 \text{ kg/m}^3, \\ E_{\mathrm{M}} = 116 \text{ GPa}, \quad \upsilon_{\mathrm{M}} = 0.34, \quad \rho_{\mathrm{M}} = 1\,200 \text{ kg/m}^3, \\ E_{\mathrm{GPL}} = 1.01 \text{ TPa}, \quad \upsilon_{\mathrm{GPL}} = 0.18, \quad \rho_{\mathrm{GPL}} = 1\,060 \text{ kg/m}^3. \end{cases} \tag{47}$$

Additionally, the upper surface of the plate is subject to a uniform pressure load given by

$$F(x, y, t) = \begin{cases} 5 \times 10^6 t, & t \leqslant 0.1, \\ 0, & t > 0.1. \end{cases} \tag{48}$$

The effects of the foundation stiffness on the maximum value of the dimensionless central deflection of the fully clamped moving bilayer plate ($n = m = 2$) for several closed-cell porosity and GPL distributions with a porosity fraction of 0.2, damping ratio of 0.0, and $V_{\mathrm{p}} = 5$ m/s are investigated, and the results are presented in Table 1. For plates without elastic foundations ($K_{\mathrm{w}} = 0$ GPa/m, $K_{\mathrm{s}} = 0$ GPa·m), the highest vertical dimensionless displacement of −9.93 is for GPL plates with non-symmetric (see the pattern B) and asymmetric porosity (see the pattern 2) distributions. The plates with symmetric GPL (see the pattern A) and symmetric porosity (see the pattern 1) distributions have the lowest transient dimensionless deflection of −8.59. When the plates are supported by an elastic foundation with $K_{\mathrm{s}} = 0.01$ GPa·s and $K_{\mathrm{w}} = 0.1$ GPa/s, the deflections reduce significantly to −6.85 and −6.17, respectively. Also, when $K_{\mathrm{s}} = 0.1$ GPa·s and $K_{\mathrm{w}} = 1$ GPa/s, the differences between the maximum values of the transient deflections of plates with different GPL and porosity distributions are negligible. The reason is that increasing the elastic foundation parameters enhances the bending rigidity of the plates and thus neutralizes the effects of the porosity and GPL distributions.

Figure 11 shows the variation of dimensionless centre deflection w/h versus dimensionless time, $T(= t/0.1)$ for the closed-cell unsymmetric porosity and GPL distribution (see the pattern B) for SSSS and CCCC boundary conditions when $\xi = 0.0$, $K_{\mathrm{s}} = 0$ GPa·m, and $K_{\mathrm{w}} = 0.01$ GPa/m. For both types of edge conditions, the plate with the larger porosity coefficient has a larger dynamic deflection than that with the smaller coefficient.

Table 1 Effects of the Winkler-Pasternak foundation parameters on dimensionless centre deflections of fully clamped axially moving bilayer plates for different GPL distribution and porosity dispersion patterns, $\widehat{A} = 2\,\%$, and $V_{\mathrm{p}} = 5$ m/s

$K_{\mathrm{s}}/(\mathrm{GPa}\cdot\mathrm{m})$	$K_{\mathrm{w}}/(\mathrm{GPa}\cdot\mathrm{m}^{-1})$	GPL distribution pattern	$1\,000 w_{\max}/h$	
			Porosity distribution pattern	
			1	2
0	0	A	−8.59	−9.31
		B	−9.31	−9.93
		C	−9.04	−9.68
	0.1	A	−7.42	−7.91
		B	−7.93	−8.45
		C	−7.75	−8.28
	1	A	−3.78	−3.85
		B	−3.83	−3.91
		C	−3.80	−3.88
0.01	0	A	−6.92	−7.31
		B	−7.32	−7.75
		C	−7.21	−7.62
	0.1	A	−6.17	−6.46
		B	−6.55	−6.85
		C	−6.44	−6.74
	1	A	−3.45	−3.53
		B	−3.55	−3.59
		C	−3.50	−3.56
0.1	0	A	−2.92	−3.00
		B	−3.06	−3.09
		C	−3.02	−3.07
	0.1	A	−2.80	−2.87
		B	−2.91	−2.96
		C	−2.89	−2.94
	1	A	−2.07	−2.11
		B	−2.12	−2.16
		C	−2.11	−2.14

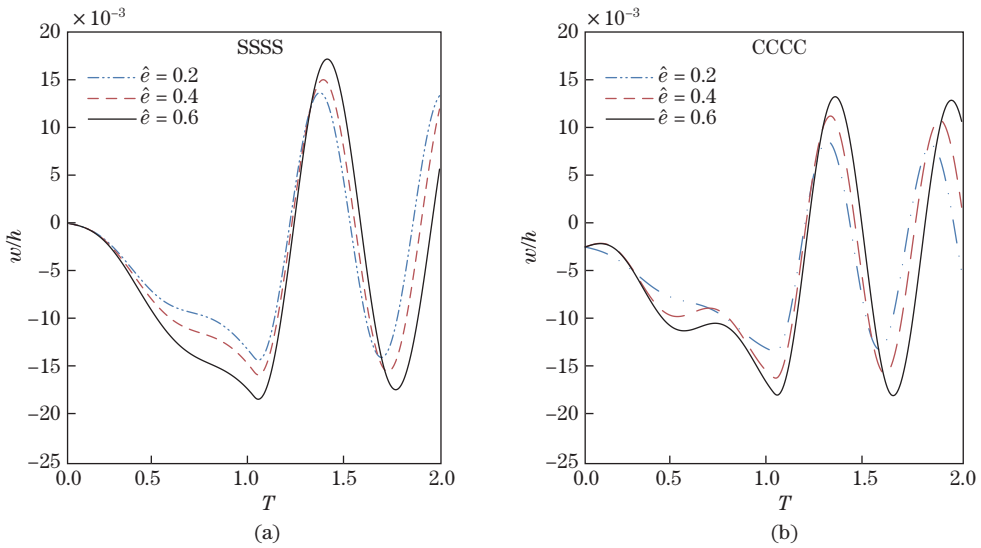

Fig. 11 Effects of porosity coefficients on the dimensionless vertical displacement of bilayer plates with asymmetric porosity and GPL distributions when $K_{\mathrm{s}} = 0$ GPa·m, and $K_{\mathrm{w}} = 0.01$ GPa/m (color online)

The dimensionless central deflections of a longitudinally moving bilayer plate with $\widehat{e} = 0.2$ (see the porosity pattern 2), $\widehat{A} = 2\,\%$ (see the GPL distribution pattern B), $\xi = 0.0$, $K_s = 0$ GPa·m, and $K_w = 0.01$ GPa/m are shown in Fig. 12 for SSSS and CCCC boundary conditions, respectively. It is evident in Fig. 12 that the dimensionless dynamic deflections of the plates increase with increases in the thickness and length (see FG indices n and m) for both boundary conditions. In comparison with the grading index n, the influence of the index m is much greater when the plate edges are clamped.

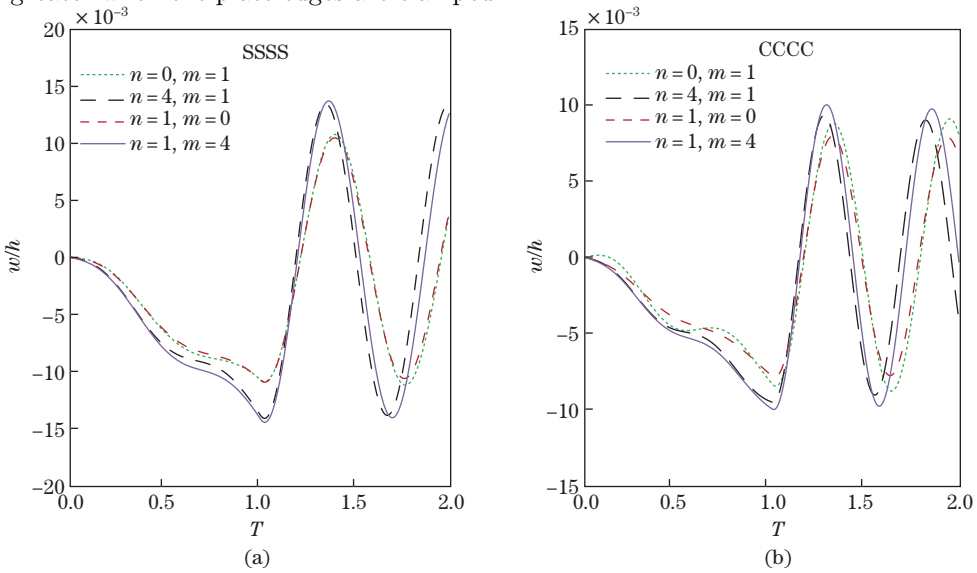

Fig. 12 Effects of gradient indices n and m on the dimensionless vertical displacement of bilayer plates with asymmetric porosity and GPL distributions when $K_s = 0$ GPa·m, and $K_w = 0.01$ GPa/m (color online)

Figure 13 illustrates how much the GPL weight fraction affects the dynamic deflection of a laminated plate ($n = 1$ and $m = 2$) with the uniform GPL distribution pattern C and the symmetric porosity pattern 1 when $\widehat{e} = 0.2$, $\xi = 0.0$, $K_s = 0$ GPa·m, and $K_w = 0.01$ GPa/m for SSSS and CCCC edge conditions. The importance of graphene nanoplatelets in improving the plate rigidity can be seen in this figure. For example, when the GPL volume fraction is doubled from 4 % to 8 %, the vertical deflection for the SSSS edge condition reduces by 14 % and by about 13.6 % for the CCCC condition.

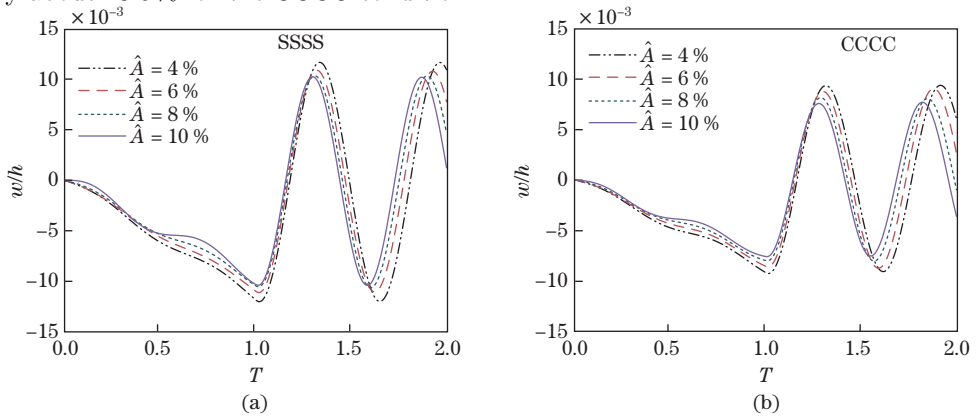

Fig. 13 Effects of GPL weight fractions on the dimensionless deflection of bilayer plates with symmetric porosity and uniform GPL distributions when $K_s = 0$ GPa·m, and $K_w = 0.01$ GPa/m (color online)

Figure 14 shows the changes in the central deflection w_s at $T = 1$ with different velocities for three GPL distributions when $\widehat{e} = 0.2$, $\xi = 0.0$, $K_s = 0$ GPa·m, and $K_w = 0.01$ GPa/m. The results show that, for both sets of edge conditions, the central deflection increases moderately until the critical velocity is reached, after which it tends to an infinity. The magnitude of the critical velocity is lower for the SSSS condition than that for the CCCC condition. It is also evident that the effects of the GPL distributions on the value of the critical velocity are small.

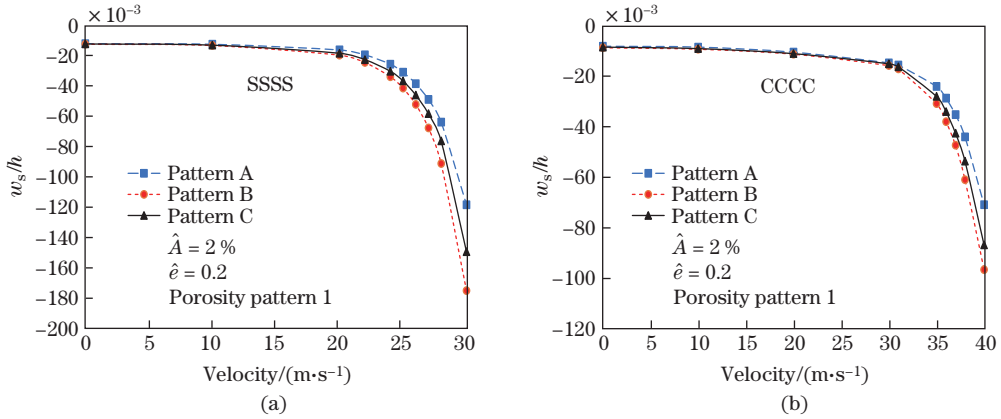

Fig. 14 Effects of velocity and GPL distributions on the dynamic deflection of moving bilayer nanocomposite plates when $K_s = 0$ GPa·m, and $K_w = 0.01$ GPa/m (color online)

The transient responses of the 2D FG/GPL plate subject to various damping ratios for SSSS and CCCC boundary conditions are shown in Fig. 15. The elastic foundation parameters are assumed as $K_s = 0$ GPa·m, $K_w = 0.01$ GPa/m and $\widehat{e} = 0.2$. It is evident from Fig. 15 that an increment in the amount of damping ratio, ξ, results in a decrease in the amplitude of deflection. This decline in the force-free zone is much more significant compared with that of the forced vibration area. It is also seen that, as the vibration period increases, the effect of the damping on the amplitude increases.

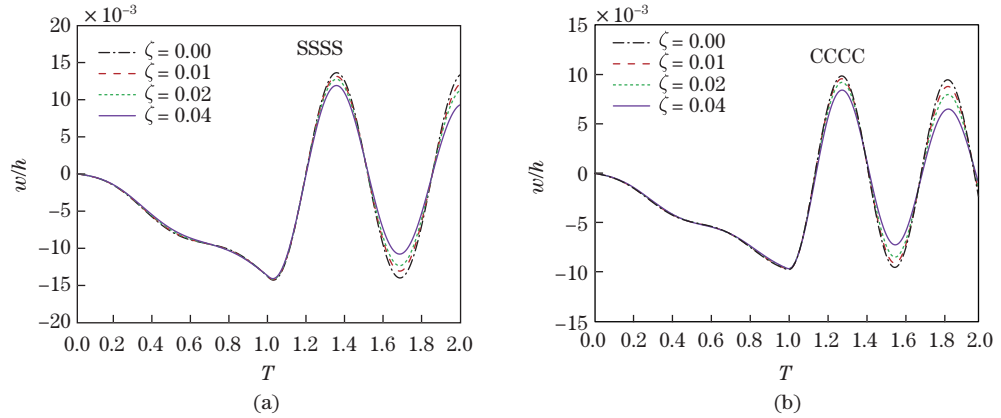

Fig. 15 Effects of damping ratios on the dynamic deflection of moving bilayer nanocomposite plates with asymmetric porosity and GPL distributions when $K_s = 0$ GPa·m, and $K_w = 0.01$ GPa/m (color online)

5 Conclusions

The dynamic analysis of 2D FG/GPL plates resting on elastic foundations with SSSS and CCCC edge conditions is studied. The equations of motion are developed based on the FSDT.

The DR and modified Newmark's integration methods are used to solve the equations. Two types of porosity and three GPL distributions are explored and compared. The effects of porosity fractions, 2D FG power indices, damping ratios, elastic foundation parameters, and porosity and GPL distributions are analyzed. The following conclusions are drawn.

(i) Graphene nanofillers can provide a significant reinforcing effect on 2D FG/GPL plates.

(ii) Material gradient indices n and m have significant effects on the response of the plates, and the axial FG index m has a greater effect on clamped plates than simply-supported plates.

(iii) Compared with asymmetric and uniform distributions, GLPs with symmetric distributions reduce the dynamic deflections more significantly.

(iv) The effects of porosity coefficients on central deflections are more significant for unsymmetric distributions.

(v) In the presence of elastic foundations, dynamic deflections reduce significantly, and the Pasternak stiffness has a greater effect than the Winkler stiffness.

(vi) A growth in the value of damping ratio leads to the decline of vibration amplitudes.

References

[1] MEHRABIAN, M. and GOLMAKANI, M. E. Nonlinear bending analysis of radial-stiffened annular laminated sector plates with dynamic relaxation method. *Computers and Mathematics with Applications*, **69**(10), 1272–1302 (2015)

[2] NARITA, Y. and TURVEY, G. J. Maximizing the buckling loads of symmetrically laminated composite rectangular plates using a layer wise optimization approach. *Proceedings of the Institution of Mechanical Engineers, Part C, Journal of Mechanical Engineering Science*, **218**(7), 681–691 (2004)

[3] TURVEY, G. J. Large deflection cylindrical bending analysis of cross-ply laminated strips. *Journal of Mechanical Engineering Science*, **23**(1), 21–29 (1981)

[4] MOLEIRO, F., MOTA-SOARES, C. M., and CARRERA, E. Three-dimensional exact hygro-thermo-elastic solutions for multilayered plates, composite laminates, fiber metal laminates and sandwich plates. *Composite Structures*, **216**, 260–278 (2019)

[5] ASHBY, M. F., EVANS, A. G., FLECK, N. A., GIBSON, L. J., HUTCHINSON, J. W., and WADLEY, H. N. G. *Metal Foams: A Design Guide*, 1st ed., Butterworth-Heinemann, Oxford, 40–54 (2000)

[6] SMITH, B. H., SZYNISZEWSKI, S., HAJJAR, J. F., SCHAFER, B. W., and ARWADE, S. R. Steel foam for structures, a review of applications, manufacturing and material properties. *Journal of Constructional Steel Research*, **71**, 1–10 (2012)

[7] LEFEBVRE, L. P., BANHART, J., and DUNAND, D. C. Porous metals and metallic foams, current status and recent developments. *Advanced Engineering Materials*, **10**(9), 775–787 (2008)

[8] HASSANI, A., HABIBOLAHZADEH, A., and BAFTI, H. Production of graded aluminum foams via powder space holder technique. *Materials and Design*, **40**, 510–515 (2012)

[9] GAO, K., LI, R., and YANG, J. Dynamic characteristics of functionally graded porous beams with interval material properties. *Engineering Structures*, **197**, 109441 (2019)

[10] GAO, K., HUANG, Q., KITIPORNCHAI, S., and YANG, J. Nonlinear dynamic buckling of functionally graded porous beams. *Mechanics of Advanced Materials and Structures*, **42**(4), 1–12 (2019)

[11] CHEN, D., YANG, J., and KITIPORNCHAI, S. Elastic buckling and static bending of shear deformable functionally graded porous beam. *Composite Structures*, **133**, 54–61 (2015)

[12] CHEN, D., YANG, J., and KITIPORNCHAI, S. Nonlinear vibration and post buckling of functionally graded graphene reinforced porous nanocomposite beams. *Composites Science and Technology*, **142**, 235–245 (2017)

[13] CHEN, D., KITIPORNCHAI, S., and YANG, J. Nonlinear free vibration of shear deformable sandwich beam with a functionally graded porous core. *Thin-Walled Structures*, **107**, 39–48 (2016)

[14] BAKSHI, S. R., LAHIRI, D., and AGARWAL, A. Carbon nanotube reinforced metal matrix composites —— a review. *International Materials Reviews*, **55**(1), 41–64 (2013)

[15] BARTOLUCCI, S. F., PARAS, J., RAFIEE, M. A., RAFIEE, J., LEE, S., KAPOOR, D., and KORATKAR, N. Graphene-aluminum nanocomposites. *Materials Science and Engineering*, **528**(27), 7933–7937 (2011)

[16] ANSARI, R. and TORABI, J. Numerical study on the buckling and vibration of functionally graded carbon nanotube-reinforced composite conical shells under axial loading. *Composites Part B, Engineering*, **95**, 196–208 (2016)

[17] RAFIEE, M. A., RAFIEE, J., WANG, Z., SONG, H., YU, Z. Z., and KORATKAR, N. Enhanced mechanical properties of nanocomposites at low graphene content. *ACS Nano*, **3**(12), 3884–3890 (2009)

[18] YANG, J., WU, H., and KITIPORNCHAI, S. Buckling and post buckling of functionally graded multilayer graphene platelet-reinforced composite beams. *Composite Structures*, **161**, 111–118 (2017)

[19] WU, H., YANG, J., and KITIPORNCHAI, S. Dynamic instability of functionally graded multilayer graphene nanocomposite beams in thermal environment. *Composite Structures*, **162**, 244–254 (2017)

[20] SONG, M., KITIPORNCHAI, S., and YANG, J. Free and forced vibrations of functionally graded polymer composite plates reinforced with graphene nanoplatelets. *Composite Structures*, **159**, 579–588 (2017)

[21] GAO, K., GAO, W., CHEN, D., and YANG, J. Nonlinear free vibration of functionally graded graphene platelets reinforced porous nanocomposite plates resting on elastic foundation. *Composite Structures*, **204**, 831–846 (2018)

[22] KITIPORNCHAI, S., CHEN, D., and YANG, J. Free vibration and elastic buckling of functionally graded porous beams reinforced by graphene platelets. *Materials and Design*, **116**, 656–665 (2017)

[23] GAO, K., GAO, W., WU, B., DI, W. U., and SONG, C. Nonlinear primary resonance of functionally graded porous cylindrical shells using the method of multiple scales. *Thin-Walled Structures*, **125**, 281–293 (2018)

[24] GAO, K., GAO, W., DI, W. U., and SONG, C. Nonlinear dynamic stability of the orthotropic functionally graded cylindrical shell surrounded by Winkler-Pasternak elastic foundation subjected to a linearly increasing load. *Journal of Sound and Vibration*, **415**, 147–168 (2018)

[25] SOFIYEV, A. H. and KURUOGLU, N. Parametric instability of shear deformable sandwich cylindrical shells containing an FGM core under static and time dependent periodic axial loads. *International Journal of Mechanical Sciences*, **101-102**, 114–123 (2015)

[26] NGUYEN, D. K., NGUYEN, Q. H., TRAN, T. T., and VAN BUI, T. Vibration of bi-dimensional functionally graded Timoshenko beams excited by a moving load. *Acta Mechanica*, **228**(1), 141–155 (2017)

[27] LEI, J., HE, Y., LI, Z., GUO, S., and LIU, D. Post-buckling analysis of bi-directional functionally graded imperfect beams based on a novel third-order shear deformation theory. *Composite Structures*, **209**, 811–829 (2019)

[28] ESMAEILZADEH, M. and KADKHODAYAN, M. Nonlinear dynamic analysis of axially moving porous FG plate subjected to local force with kinetic dynamic relaxation method. *Computer Methods in Materials Science*, **18**(1), 18–28 (2018)

[29] WANG, Y. Q. and YANG, Z. Nonlinear vibrations of moving functionally graded plates containing porosities and contacting with liquid: internal resonance. *Nonlinear Dynamics*, **90**(2), 1461–1480 (2017)

[30] LI, Y. H., DONG, Y. H., QIN, Y., and LV, H. W. Nonlinear forced vibration and stability of an axially moving viscoelastic sandwich beam. *International Journal of Mechanical Sciences*, **138-139**, 131–145 (2018)

[31] ZHOU, Y. F. and WANG, Z. M. Dynamic instability of axially moving viscoelastic plate. *European Journal of Mechanics-A/Solids*, **73**, 1–10 (2019)

[32] TAKABATAKE, H. A simplified analysis of rectangular floating plates subjected to moving loads. *Ocean Engineering*, **97**, 37–47 (2015)

[33] GAO, K., GAO, W., WU, D., and SONG, C. Nonlinear dynamic characteristics and stability of composite orthotropic plate on elastic foundation under thermal environment. *Composite Structures*, **168**, 619–632 (2017)

[34] VANDO, T., NGUYEN, D. K., DUC, N. D., DOAN, D. H., and BUI, T. Q. Analysis of bi-directional functionally graded plates by FEM and a new third-order shear deformation plate theory. *Thin-Walled Structures*, **119**, 687–699 (2017)

[35] SAHMANDI, S., AGHDAM, M. M., and RABCZUK, T. Nonlocal strain gradient plate model for nonlinear large-amplitude vibrations of functionally graded porous micro/nano-plates reinforced with GPLs. *Composite Structures*, **198**, 51–62 (2018)

[36] MOJAHEDIN, A., JABBARI, M., KHORSHIDVAND, A. R., and ESLAMI, M. R. Buckling analysis of functionally graded circular plates made of saturated porous materials based on higher order shear deformation theory. *Thin-Walled Structures*, **99**, 83–90 (2016)

[37] ROBERTS, A. P. and GARBOCZI, E. J. Elastic moduli of model random three-dimensional closed-cell cellular solids. *Acta Materialia*, **49**(2), 189–197 (2001)

[38] EBRAHIMI, F. and DABBAGH, A. Vibration analysis of multi-scale hybrid nanocomposite plates based on a Halpin-Tsai homogenization model. *Composites Part B: Engineering*, **173**, 106955 (2019)

[39] ARANI, A. G., HAGHPARAST, E., and BABAAKBARZAREI, H. Nonlocal vibration of axially moving graphene sheet resting on orthotropic visco-Pasternak foundation under longitudinal magnetic field. *Physica B: Condensed Matter*, **495**, 35–49 (2016)

[40] TURVEY, G. J. and SALEHI, M. Elastic-plastic large deflection response of pressure loaded circular plates stiffened by a single diametral stiffener. *Thin-Walled Structures*, **46**, 991–1002 (2008)

[41] GOLMAKANI, M. E. and KADKHODAYAN, M. Large deflection thermoelastic analysis of functionally graded stiffened annular sector plates. *International Journal of Mechanical Sciences*, **69**, 94–106 (2013)

[42] REZAEI-MOJDEHI, A., DARVIZEH, A., BASTI, A., and RAJABI, H. Three dimensional static and dynamic analysis of thick functionally graded plates by the meshless local Petrov-Galerkin (MLPG) method. *Engineering Analysis with Boundary Elements*, **35**(11), 1168–1180 (2011)

[43] AN, C. and SU, J. Dynamic response of clamped axially moving beams: integral transform solution. *Applied Mathematics and Computation*, **218**(2), 249–259 (2011)

[44] CONG, P. H. and DUC, N. D. New approach to investigate the nonlinear dynamic response and vibration of a functionally graded multilayer graphene nanocomposite plate on a viscoelastic Pasternak medium in a thermal environment. *Acta Mechanica*, **229**(9), 3651–3670 (2018)